

Bipolar Thermoelectric Josephson Engine

Gaia Germanese,^{1,2} Federico Paolucci,¹ Giampiero Marchegiani,³ Alessandro Braggio,¹ and Francesco Giazotto^{1,*}

¹*NEST, Istituto Nanoscienze-CNR and Scuola Normale Superiore, I-56127 Pisa, Italy*

²*Dipartimento di Fisica dell'Università di Pisa, Largo Pontecorvo 3, I-56127 Pisa, Italy*

³*Quantum Research Centre, Technology Innovation Institute, Abu Dhabi, UAE*

Thermoelectric effects in metals are typically small due to the nearly-perfect particle-hole (PH) symmetry around their Fermi surface [1, 2]. Despite being initially considered paradoxical [3], thermopower effects [4–8] and linear thermoelectricity [9] in superconducting systems were identified only when PH symmetry is explicitly broken [10–14]. Here, we experimentally demonstrate that a superconducting tunnel junction can develop a very large bipolar thermoelectric effect in the presence of a nonlinear thermal gradient thanks to *spontaneous* PH symmetry breaking [15]. Our junctions show a maximum thermovoltage of $\pm 150 \mu\text{V}$ at $\sim 650 \text{ mK}$, directly proportional to the superconducting gap. Notably, the corresponding Seebeck coefficient of $\pm 300 \mu\text{V/K}$ is roughly 10^5 times larger than the one expected for a normal metal at the same temperature [16, 17]. Moreover, by integrating our junctions into a Josephson interferometer, we realize a bipolar thermoelectric Josephson engine (BTJE) [18] with phase-coherent thermopower control [19]. When connected to a generic load, the BTJE generates a phase-tunable electric power up to $\sim 140 \text{ mW/m}^2$ at subKelvin temperatures. In addition, our device implements the prototype for a persistent thermoelectric memory cell, written or erased by current injection [20]. We expect that our findings will trigger thermoelectricity in PH symmetric systems, and will lead to a number of groundbreaking applications in superconducting electronics [21], cutting-edge quantum technologies [22–24] and sensing [25].

Thermoelectricity is the capability of materials to directly convert temperature gradients into an electrical power [1, 2]. Specifically, a thermoelectric element can supply a short-circuit current (*Peltier regime*) or generate an open-circuit voltage (*Seebeck regime*) whose sign is determined by the sign of the dominant carriers and temperature gradient. All systems characterized by strong PH symmetry, such as normal metals and superconductors, show poor thermoelectric effects [16, 17]. Moreover, thermoelectricity in superconductors is also screened by the dissipationless motion of Cooper pairs [3], thereby only thermo-phase effects can be eventually observed [4, 6–8]. Yet, a pure local thermoelectric effect can only be generated in superconducting tunnel junctions with suppressed Josephson coupling by explicitly breaking the PH symmetry [9–14], whereas non-local thermoelectricity can be detected in superconducting hybrid structures [26–31]. These intrinsic limitations hindered so far the implementation of superconducting thermoelectric devices in quantum technologies, such as radiation detectors, switches, memories, and engines. Indeed, despite great theoretical efforts [32–34], the experimental realization of efficient solid-state heat engines is still limited to InAs/InP quantum-dots [35], molecular systems [36] and silicon tunnel transistors [37].

Here, we report the experimental observation of an astounding bipolar thermoelectric effect in tunnel junctions between two different superconductors subject to nonlinear temperature gradients [15]. Its unique bipolarity stems from the equal possibility for *both* directions of the thermocurrent or polarities of the thermovoltage at a *given* temperature gradient. The effect is determined by nonequilibrium *spontaneous* breaking of PH symmetry and can be phase-controlled in a Josephson interferometer [19]. We exploit these features to realize a bipolar thermoelectric Josephson engine (BTJE) [18], which finds immediate application in superconducting quantum technology [20].

The core of the BTJE is a S_1IS_2 tunnel junction between two different Bardeen-Cooper-Schrieffer superconductors with suppressed Josephson coupling (where S_1 and S_2 have zero-temperature energy gaps $\Delta_{0,1} > \Delta_{0,2}$, and I stands for an insulator). At thermal equilibrium (i.e., for identical temperatures $T_1 = T_2 = T_{\text{cold}}$), the junction is dissipative, and cannot generate power [32] (see top panel of Fig. 1a). By contrast, in the presence of a suitable thermal bias (i.e., $T_1 = T_{\text{hot}} > T_2 = T_{\text{cold}}$), the junction is expected to yield thermoelectricity [15]. As we shall show, this structure may spin an electrical motor in both directions for a *given* thermal gradient depending on the polarization history of the junction, as sketched in the bottom panel of Fig. 1a.

Our implementation of the BTJE is shown by the false-color scanning electron micrograph in Fig. 1b. It consists of a double-loop superconducting quantum interference device (SQUID) [38, 39], where S_1 (red, Al) is coupled to S_2 (blue, Al/Cu bilayer) through three insulating AlO_x tunnel junctions. In this configuration, the three S_1IS_2 junctions constitute a Josephson interferometer, which is used to phase-control the thermoelectric generation [19] via fine tuning of the dissipationless supercurrent. In particular, a double-loop SQUID guarantees a more effective suppression of the Josephson coupling with respect to a conventional single-loop two-junction interferometer [38, 39], thereby allowing

* francesco.giazotto@sns.it

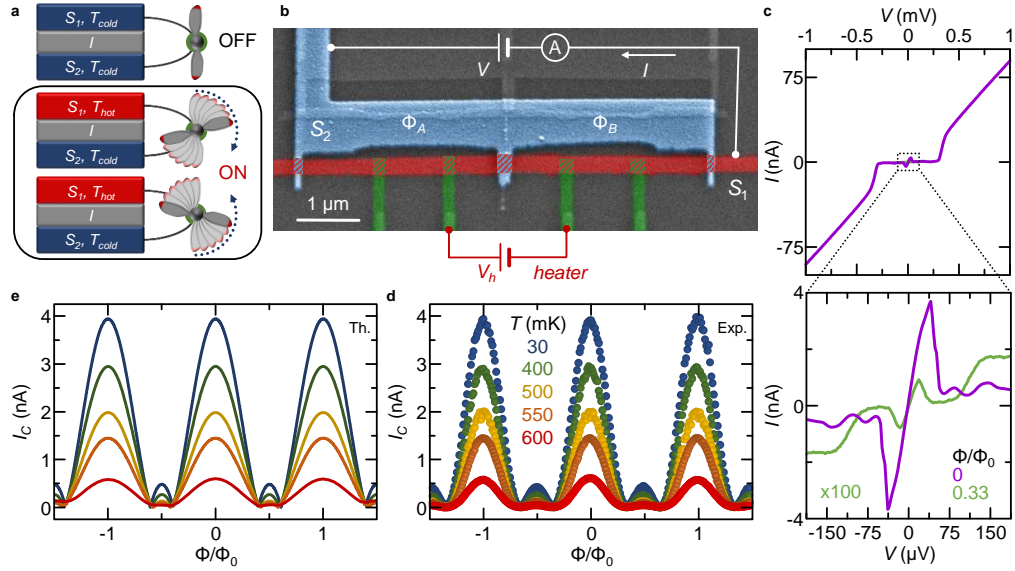


FIG. 1. **Bipolar thermoelectric Josephson engine.** **a** Scheme of the bipolar thermoelectric Josephson engine (BTJE): two different superconductors S_1 and S_2 (with zero-temperature energy gaps $\Delta_{0,1} > \Delta_{0,2}$) are tunnel-coupled through a thin insulating layer (grey, I). The S_1IS_2 junction is predicted to generate power when S_1 is kept at a higher temperature than S_2 (i.e., $T_1 = T_{hot} > T_2 = T_{cold}$). Remarkably, this structure can produce both *positive* and *negative* thermovoltage for the same thermal gradient imposed across the junction. **b** Pseudo-color scanning electron micrograph of a typical BTJE. An aluminum island (S_1 , red) is tunnel coupled through three AlO_x barriers to a Cu/Al bilayer (S_2 , blue) thus realizing a double-loop SQUID. Additional tunnel-coupled Al electrodes (green) serve as Joule heaters for S_1 . Replicas resulting from the shadow-mask fabrication procedures are also visible (see Methods for details). The charge transport properties of the double-loop SQUID were investigated in a two-wire configuration by recording the tunneling current (I) while a voltage (V) was applied. Φ_A and Φ_B represent the magnetic fluxes linked to each loop, so that the total flux through the interferometer is $\Phi = \Phi_A + \Phi_B$. **c** Top panel: current (I) versus voltage (V) characteristics measured at 30 mK for $\Phi = 0$ (violet) and $\Phi = 0.33\Phi_0$ (green). Bottom panel: blow-up of the IV characteristics around $V = 0$. **d** Experimental Josephson critical current (I_C) of the double-loop interferometer vs Φ measured for different values of bath temperature. **e** Theoretical modulations of I_C vs Φ calculated with the model presented in the SI.

an improved control of the thermoelectric effect. Moreover, S_1 is also equipped with several superconducting tunnel junctions (green, Al) operated as Joule heaters to establish the necessary temperature gradient across the structure. The structure fabrication details are provided in the Methods section.

Investigation of charge transport in the BTJE is performed first in the absence of a temperature gradient (i.e., for $T_1 = T_2 = T$). Figure 1c shows the 2-wire SQUID current (I) versus voltage (V) characteristics measured at 30 mK for two representative values of magnetic flux (Φ). The SQUID switches to the normal-state characteristic at $V = \pm(\Delta_{0,1} + \Delta_{0,2})/e \simeq \pm 300 \mu V$ (with e the electron charge) displaying a total junction resistance $R_T \sim 9 \text{ k}\Omega$ (top panel). Moreover, the Josephson critical current, manifesting itself as a peak around zero bias, is significantly modulated by Φ (bottom panel). The interference patterns of the critical current (I_C) recorded at different values of bath temperature are shown in Fig. 1d. In agreement with our model (see Fig. 1e, and SI for the model details), the double-loop geometry allows an effective and fine phase-tuning of the SQUID transport properties, and a maximum suppression of the supercurrent up to $\sim 1.75\%$ of the zero-flux value for $\Phi = 0.33\Phi_0$.

Bipolar thermoelectric effect

To assess the predicted bipolar thermoelectric effect [15], we measured the subgap IV characteristics of the BTJE at a bath temperature of 30 mK while directly injecting power (P_{in}) in S_1 . Power injection raises the temperature of S_1 above the bath value, thereby generating a thermal gradient across the interferometer (i.e., $\delta T = T_1 - T_2 > 0$) [40, 41]. Since the Josephson coupling is detrimental for thermoelectricity [18], we flux-biased the SQUID at $\Phi = 0.33\Phi_0$ in order to minimize the supercurrent flowing through the interferometer. For finite input power (i.e., for $P_{in} \geq 10 \text{ pW}$), the subgap quasiparticles current flows against the bias voltage ($IV < 0$), thus displaying the *absolute negative conductance* (ANC) [42, 43], which signals thermoelectric generation (see Fig. 2a) [15]. Differently from other known thermoelectric effects [1], the BTJE shows *bipolar* power generation, i.e., the ANC appears for both positive and

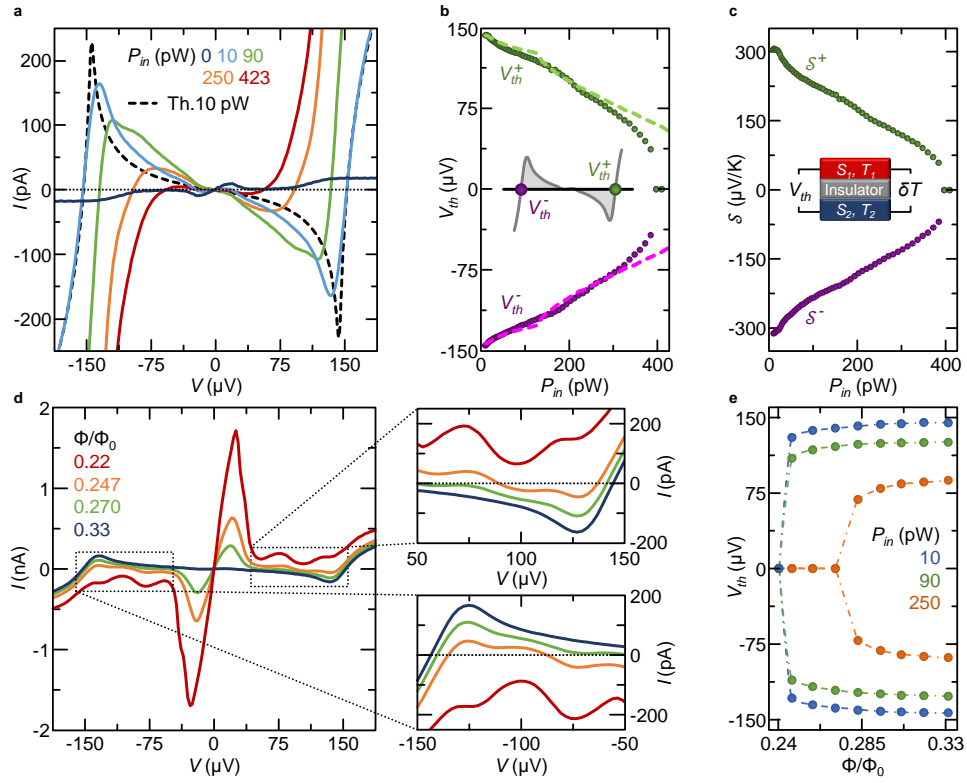


FIG. 2. **Bipolar thermoelectric effect.** **a** Subgap current (I) vs voltage (V) characteristics of the SQUID measured at $\Phi = 0.33\Phi_0$ for different values of the input power (P_{in}) injected in S_1 . In the presence of a thermal bias, the interferometer shows an *absolute negative* conductance (ANC) for both polarities of V . The black dashed line is the result from the theory for a single junction [15] calculated at 10 pW. The temperature bias across the BTJE is deduced by fitting the experimental IV curves with the theory (see SI for details). **b** Thermovoltage (V_{th}) vs P_{in} recorded at $\Phi = 0.33\Phi_0$ (dots). Dashed lines correspond to the theory [15]. Due to intrinsic electron-hole symmetry, the system provides both *positive* (V_{th}^+ , green) and *negative* (V_{th}^- , purple) thermovoltage for any given P_{in} . **c** Seebeck coefficient (\mathcal{S}) vs P_{in} extracted from the data shown in panel b according to the calibration presented in the SI. In the presence of thermoelectricity, the value of \mathcal{S} monotonically decreases by increasing P_{in} . **d** Subgap IV characteristics of the SQUID measured at $P_{in} = 10$ pW for selected values of Φ . Top (bottom) inset shows a magnification of the current close to V_{th}^+ (V_{th}^-). **e** V_{th} vs Φ measured for different values of P_{in} . Dash-dotted lines are guides to the eye. All measurements were performed at a bath temperature of 30 mK.

negative values of V at *given* temperature gradient. These unique anti-symmetric thermoelectric IV characteristics [$I(-V) = -I(V)$] stem from PH symmetry of the two superconducting leads. In general, the experimental IV traces are in agreement with the theoretical behavior obtained by computing the quasiparticle current (black dashed line) in the presence of a non-linear temperature gradient [15] (see Methods for details). When the input power is too large (i.e., for $P_{in} \gtrsim 400$ pW), the thermoelectricity vanishes, and the IV characteristics show the conventional dissipative behavior (see the red curve in Fig. 2a). This power dependence is highlighted by the thermovoltage (V_{th}), i.e., the finite potential drop occurring across the BTJE when $I(V_{th}) = 0$. For linear thermoelectricity this quantity corresponds to the Seebeck voltage [32]. In our measurements, the thermovoltage obtains values as large as $\sim \pm 150$ μV for the lowest heating power of 10 pW, in good agreement with theory (see dashed line in Fig. 2b). In contrast to linear thermoelectricity, by increasing P_{in} (and therefore at larger temperature gradients) yields a monotonic reduction of the absolute value of both polarities of V_{th} , until reaching full suppression around 400 pW.

It is common to evaluate the performance of a thermoelectric element through the Seebeck coefficient, defined as $\mathcal{S} = V_{th}/\delta T$. The resulting bipolar Seebeck coefficient vs P_{in} is shown in Fig. 2c (see SI for details). For the BTJE, \mathcal{S} can be as high as ± 300 $\mu V/K$ at $P_{in} = 10$ pW (corresponding to a temperature of $\simeq 650$ mK in S_1), which is near to the maximum theoretically achievable with our materials [15, 18]. We stress that the above value is almost 10^5 times larger than the Seebeck coefficient of aluminum [$\mathcal{S}_{Al}(650 \text{ mK}) \simeq -3.8$ nV/K] [16, 17] computed through the Mott-Jones equation (see Methods for details).

To demonstrate the interplay between our thermoelectric effect and the Josephson coupling [19], we measured the IV characteristics at a given input power ($P_{in} = 10$ pW) for different values of the magnetic flux piercing the interferometer. As expected, the thermoelectric effect is strongly suppressed for both voltage polarities in the presence

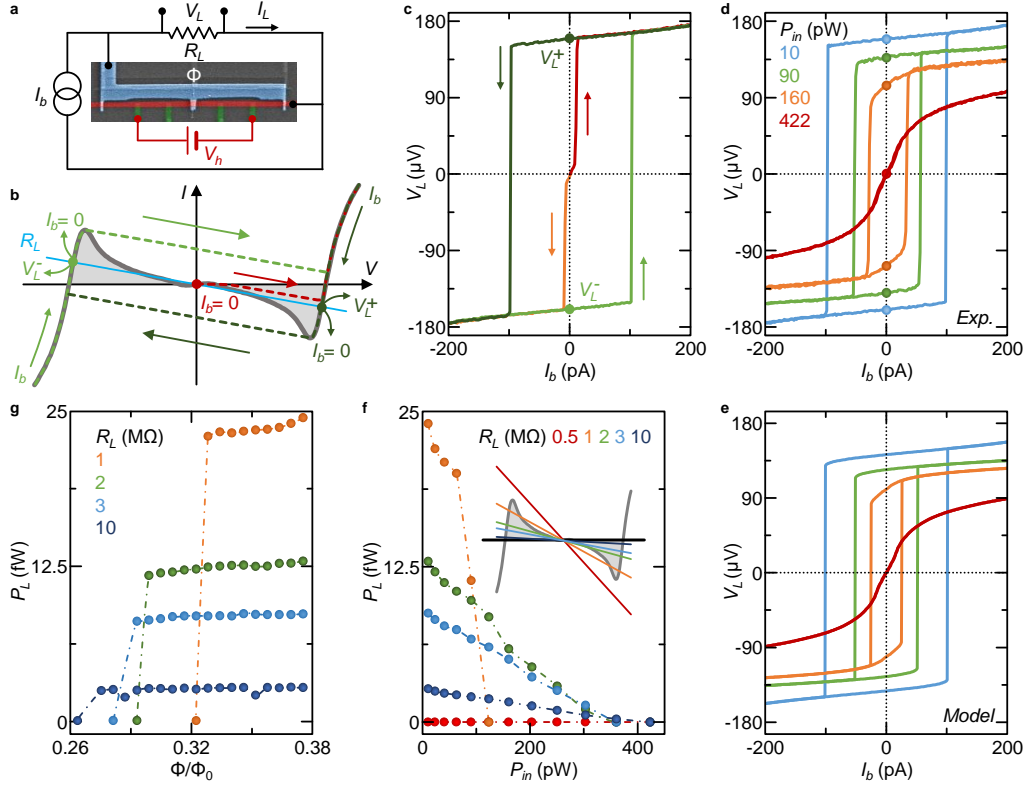


FIG. 3. Low temperature behavior of the BTJE. **a** Scheme of the electronic circuit used to demonstrate power production. The Joule heaters are powered through a floating voltage source (V_h). A dc current source (I_b) biases the parallel connection of the interferometer and a load resistor (R_L) while recording the voltage drop V_L occurring across R_L . **b** Sketch of thermoelectric current (I) vs voltage (V) characteristic where a resistive load (blue line) is superimposed. A typical hysteresis loop of the load voltage (V_L) is also represented (green dashed curves) together with the thermovoltages (V_L^+ or V_L^-) corresponding to zero biasing current (i.e., $I_b = 0$). Grey areas represent *thermoactive* regions. **c** V_L vs I_b recorded with $R_L = 2$ M Ω at $P_{in} = 10$ pW and $\Phi = 0.33\Phi_0$. The engine can be ignited by ramping I_b from zero towards either positive (red) or negative (orange) values. Thermovoltages measured at $I_b = 0$ (green dots, V_L^+ or V_L^-) prove power production in the system, i.e., the realization of the *engine*. The thermovoltage polarity can be changed by ramping I_b to large values (green curves). **d** V_L vs I_b characteristics measured with $R_L = 2$ M Ω and $\Phi = 0.33\Phi_0$ for selected values of input power. **e** Results from the model for the same parameters as in panel d (see SI for details). **f** Engine output power (P_L) vs input power (P_{in}) at $\Phi = 0.33\Phi_0$ for different values of R_L . Inset: characteristics of different loads (colored lines) superimposed to a typical BTJE thermoelectric IV curve (grey). **g** P_L vs Φ at $P_{in} = 10$ pW for different values of R_L . Dash-dotted lines in panels f and g are guides to the eye. All measurements were performed at a bath temperature of 30 mK.

of a sizeable Josephson current (see Fig. 2d). Specifically, at low P_{in} , thermoelectricity vanishes for $\Phi \simeq 0.24\Phi_0$, corresponding to $I_C \simeq 850$ pA (see Fig. 2e). This behavior proves full Φ -control of V_{th} until its complete suppression [19] and is unique to the BTJE. It is noteworthy that Josephson coupling affects more easily thermoelectricity when it is weaker, as is happens at larger injected power (see orange curve in Fig. 2e). As discussed above, P_L is reduced by raising P_{in} , due to the peculiar nonlinearity of the thermoelectric effect. As a result, even small values of the Josephson current shunting the interferometer can suppress the thermoelectric generation at a large temperature bias.

Operation of the BTJE

Let us now analyze the behavior of the interferometer when performing as an engine. The electronic circuit used to operate the SQUID as a thermoelectric engine [18] is schematically shown in Fig. 3a, where the device is connected in parallel to a load resistor (R_L), and biased by a dc current (I_b). In the presence of a thermal gradient ($P_{in} > 0$), the combined system BTJE $\parallel R_L$ exhibits up to three metastable states, as shown by the colored dots in Fig. 3b. These solutions are obtained by the intersection between the IV characteristic of the SQUID (grey curve) and one of the resistive load (cyan line). Initially, the system is in the PH symmetric point, and the most favourable solution

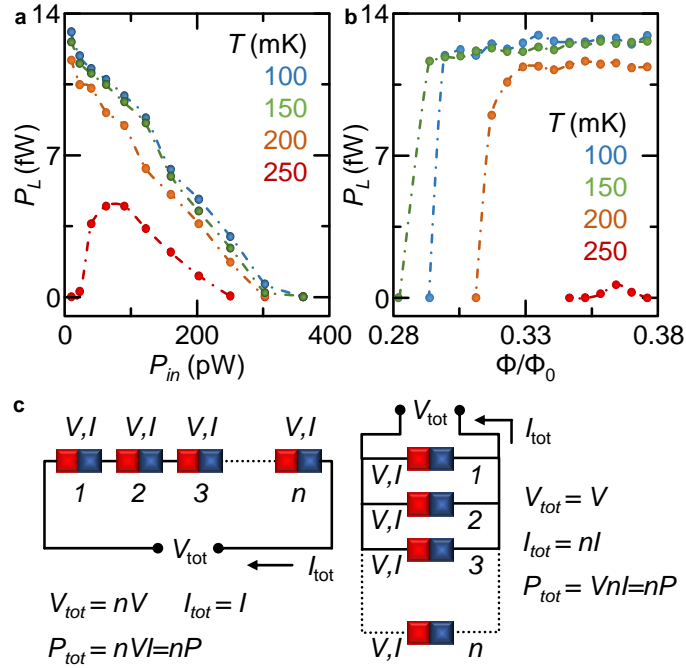


FIG. 4. **Temperature dependence of the BTJE.** **a** Output power P_L at $\Phi = 0.33\Phi_0$ and $R_L = 2 \text{ M}\Omega$ vs input power P_{in} for different values of bath temperature T . **b** P_L at $P_{in} = 10 \text{ pW}$ and $R_L = 2 \text{ M}\Omega$ vs Φ for selected values of T . Dash-dotted lines in panels a and bare guides to the eye. **c** Schematic representation of a series (left) and parallel (right) connection of n S₁IS₂ thermoelectric elements. The series connection yields a total voltage $V_{tot} = nV$ (with V the voltage drop occurring across each element) and a total current $I_{tot} = I$ (with I the current flowing through each element), whereas the parallel connection provides $V_{tot} = V$ and $I_{tot} = nI$. Therefore, both configurations generate an output power $P_{tot} = I_{tot}V_{tot} = nIV = nP$ (P denotes the power produced by a single element).

is $V = 0$ (red dot). Therefore, the engine is off ($I = 0$). The BTJE is ignited through a bias current (I_b), and its polarity can be selected by the sign of I_b . Indeed, positive (negative) values of I_b rigidly shift up (down) the load curve upon the interferometer IV characteristic thus selecting the positive (negative) thermoactive branch of the BTJE. After ignition, the engine yields a voltage drop V_L^+ (or V_L^-) across R_L at $I_b = 0$. By decreasing (increasing) the bias current, the load curve can intercept the BTJE characteristic only in the negative (positive) thermoactive branch thereby inverting the operation polarity of the engine. Details of the circuit operation are provided in the SI.

The bipolar power generation of the BTJE leads to the experimental V_L vs I_b traces shown in Fig. 3c for $R_L = 2 \text{ M}\Omega$, $P_{in} = 10 \text{ pW}$ and $\Phi = 0.33\Phi_0$. Indeed, the engine is ignited by a positive (negative) current bias, represented with a red (orange) curve and, then, it is able to generate positive (negative) voltages across R_L (i.e., V_L^+ and V_L^-) even when the bias is switched off $I_b = 0$. Remarkably, by using the Bogoliubov criterium for phase transitions [47, 48], the hysteretic behaviour of $V_L(I_b)$ implicitly proves that the bipolar thermoelectric effect stems from *spontaneous* breaking of PH symmetry in the system.

Since thermoelectricity strongly depends on the amplitude of the thermal gradient, P_{in} has a marked impact on the $V_L(I_b)$ characteristics (see Fig. 3d). In particular, the absolute values of both the voltage developed across R_L and the bias current corresponding to polarity inversion of V_L are reduced by rising P_{in} . Yet, at large P_{in} values, the hysteretic behavior disappears, and the BTJE turns off, since the thermoelectric effect vanishes in the presence of sizable temperature gradients (see Fig. 2a). The above behavior is in full agreement with the solution of the circuitual model describing our experiment (see Fig. 3e, and SI for details). We also emphasize that thanks to its hysteretic character this circuit directly implements a volatile thermoelectric *memory cell* with the capability to be written/erased by current pulses [20].

Figure 3f shows the output power, defined as $P_L = (V_L^\pm)^2/R_L$, produced by the BTJE on different load resistors vs P_{in} at 30 mK, and $\Phi = 0.33\Phi_0$. In full agreement with the thermovoltage behavior, P_L decreases by rising the temperature gradient (with input power). On the one hand, the engine produces more power for lower values of R_L , since V_L is almost independent of R_L . In particular, the BTJE delivers powers as large as $P_L \sim 24 \text{ fW}$ for $R_L = 1 \text{ M}\Omega$, which corresponds to a surface power density of about 140 mW/m^2 . On the other hand, the thermal gradient (input power) operation window of the BTJE narrows by decreasing R_L , since the load curves cease to intercept the

SQUID IV characteristics even at the lowest values of P_{in} . Indeed, the engine is not able to sustain power if the load resistor is too low (we measured $R = 0.5 \text{ M}\Omega$ for the present device, see the inset of Fig. 3f). The phase tunability of the thermoelectric effect allows to control power production of the BTJE with Φ , as shown in Fig. 3g. The value of P_L can be controlled over a larger range of amplitudes for smaller resistive loads at the cost of power generation occurring in a narrower flux window. By contrast, large loads lead to reduced power tunability although occurring over a larger operation range in Φ .

We now discuss the impact of bath temperature (T) on the BTJE performance. Figure 4a shows the dependence of P_L on P_{in} measured at different temperatures for $R_L = 2 \text{ M}\Omega$, and $\Phi = 0.33\Phi_0$. By rising T , the output power generally decreases, and the BTJE operation range in P_{in} narrows, since the bipolar thermoelectric effect weakens at higher temperatures. Yet, the BTJE operates up to 250 mK, corresponding to $\sim 40\%$ of the critical temperature of S_2 . Interestingly, P_L is non-monotonic in P_{in} , and this can be better appreciated at $T = 250 \text{ mK}$. The above behavior with the temperature may be ascribed to a sizable change of the electron-phonon thermalization in S_1 with bath temperature [40, 44] and, thereby, to the resulting difference in the P_{in} dependence of the thermal gradient established across the BTJE joined to the nonlinearity of bipolar thermoelectricity. Moreover, the Φ -tunability of the output power turns out to be more efficient at higher values of bath temperature, as shown in Fig. 4b. Indeed, a weaker thermoelectric effect is more sensitive to the magnetic flux (see also Fig. 2e). Therefore, depending on the specific application, the operation temperature of the BTJE can be chosen in order to maximise the output power (i.e., at low bath temperature) or the flux sensitivity (i.e., at high bath temperature).

Discussion

Our work presents a paradigmatic fully-bipolar thermoelectric effect occurring in superconducting tunnel junctions, thereby unveiling the possibility for significant thermoelectricity also in PH symmetric systems [15]. Differently from conventional linear thermoelectric effects [1, 2], when subject to a large thermal bias, our Josephson junctions show a remarkable *bipolar* power generation, which stems from a non equilibrium-induced *spontaneous* PH symmetry breaking. Indeed, the sign of the generated voltage depends on the bias history of the system for a given thermal gradient. In particular, our superconducting junctions yield thermovoltages up to about $\pm 150 \text{ }\mu\text{V}$ corresponding to a non-linear Seebeck coefficient $\mathcal{S} \simeq \pm 300 \text{ }\mu\text{V/K}$. Strikingly, this value is $\sim 10^5$ times larger than the linear Seebeck coefficient of a normal metal at the same temperature. The integration of thermally-biased superconducting tunnel junctions in a properly designed Josephson interferometer [38, 39] allows fine control of the thermoelectric effect via an external magnetic flux [19], owing to the strong competition between the Josephson coupling and thermoelectricity. We then exploit the resulting bipolar thermoelectric Josephson engine [18] to power a generic load resistor kept at room temperature. In this configuration, a direct current injection has the double role of igniting the engine, and selecting its output polarity. The BTJE delivers up to $\sim 24 \text{ fW}$ corresponding to an areal output power density $\sim 140 \text{ mW/m}^2$ or, equivalently, to a power per conductance unit of $\sim 190 \text{ pW/S}$. In addition, the circuit controlling the BTJE defines a hysteretic IV characteristic, which can be exploited to realize a potentially-fast volatile thermoelectric memory cell written or erased by a bias current [20].

In terms of sizable-power thermoelectric production, an on-chip generator could consist of an array of several BTJEs connected in series or parallel, as shown in Fig. 4c. We stress that the series connection can advantageously be realized only by exploiting the described *bipolar* device, since otherwise the voltage drop across each element would not simply add. Indeed, in conventional unipolar thermoelectric devices this configuration can only work by using a sequence of n and p materials. Here, the same junction takes spontaneously the role of the two elements [18]. The total output power is $P_{tot} = nP$ in both configurations (with n the number of elements), and while the series connection ensures high voltage production ($V_{tot} = nV$), the parallel connection guarantees high current generation ($I_{tot} = nI$). We also note that the BTJE already exploits the parallel connection of three thermoelectric elements (i.e., the S_1IS_2 junctions) to increase the total output current (see Fig. 1b).

From the side of possible applications, the BTJE might find direct utilization in superconducting quantum technology [22–24] through the implementation of engines, power generators, electronic devices [21], memories, radiation sensors [25] and switches. Yet, alternative realizations of the BTJE might exploit extended Josephson tunnel junctions immersed in a parallel magnetic field [49], or subject to spin-filtering in order to suppress the Josephson coupling [10–14]. Finally, we stress that the above bipolar thermoelectric effect is expected to occur in several physical systems characterized by intrinsic PH symmetry in the presence of a nonlinear temperature gradient: thermoelectricity, indeed, requires only tunnel junctions where the hot and cold electrodes possess a *gapped* and *monotonically-decreasing* density of states, respectively [15]. Our study is then pivotal for groundbreaking investigations of nonlinear thermoelectric effects in different systems ranging from semiconductors and low-dimensional electronic materials to high-temperature superconductors and topological insulators.

METHODS

Devices fabrication

The devices were nanofabricated by a single electron-beam lithography (EBL) step, three-angle shadow-mask metals deposition onto a Si wafer covered with 300nm-thick thermally-grown SiO_2 through a suspended bilayer resist mask, and in-situ metal oxidation to define the tunnel junctions. The evaporation and oxidation processes were performed in an ultra-high vacuum (UHV) electron-beam evaporator with a base pressure of 10^{-11} Torr. At first, the superconducting heaters were deposited by evaporating a 12-nm-thick aluminum film at an angle of 30° . Then, the film was exposed to 1 Torr of O_2 for 20 minutes to create the AlO_x layer forming the tunnel barriers. Subsequently, the 14-nm-thick aluminum island (S_1) was evaporated at 0° and oxidized in 1 Torr of pure oxygen atmosphere for 30 minutes to realize the tunnel junctions of the SQUID. Finally, an aluminum/copper bilayer (S_2 , $t_{Al} = 14$ nm and $t_{Cu} = 11$ nm) was deposited at an angle of -30° to form the remaining arms of the interferometer.

Measurement set-up

All measurements were performed in a filtered $\text{He}^3\text{-He}^4$ dry dilution refrigerator (Triton 200, Oxford Instruments) at different bath temperatures ranging from 30 mK to 600 mK. The transport properties of the double-loop SQUID were recorded in a standard two-wire configuration by applying a voltage bias through a floating source (GS200, Yokogawa), and by measuring the current with a room-temperature current pre-amplifier (Model 1211, DL Instruments). The Joule heaters were energized by a battery-powered voltage source (SIM 928, Stanford Research Systems). Finally, the magnetic flux piercing the SQUID was provided by a superconducting solenoid driven by a low-noise current source (GS200, Yokogawa).

Device parameters

The areas of the central, left and right junction are obtained from the SEM picture of the device, and get the value $A_0 = 8.5 \times 10^{-2} \mu\text{m}^2$, $A_A = 4.5 \times 10^{-2} \mu\text{m}^2$ and $A_B = 4 \times 10^{-2} \mu\text{m}^2$, respectively. The resulting total area of the junctions composing the interferometer is $A_{int} = A_0 + A_A + A_B = 1.7 \times 10^{-1} \mu\text{m}^2$ (in good agreement with the SQUID interference patterns). The normal-state tunnel resistance of all tunnel junctions is obtained from the experimental IV characteristics. The tunnel resistance of the double-loop interferometer results from the parallel connection of its three junctions, thus it reads $R_T = \frac{R_0 R_A R_B}{R_0 R_A + R_0 R_B + R_A R_B} \simeq 9 \text{ k}\Omega$, where R_0 , R_A and R_B are the normal-state resistances of the central, left and right junction, respectively. The normal-state resistance of the two tunnel junction Joule heaters is $R_{h1} \simeq 25.2 \text{ k}\Omega$, and $R_{h2} \simeq 26.6 \text{ k}\Omega$, respectively. The shown two-wire characteristics include the resistance of the cryostat filters. Each line contributes to the transport with a resistance $R_f = 1.1 \text{ k}\Omega$. The S_1 island is characterized by a zero-temperature energy gap $\Delta_{0,1} \simeq 220 \mu\text{eV}$, thus providing a superconducting coherence length $\xi_{S1} = \sqrt{\hbar D_{Al}/\Delta_{0,1}} \simeq 82 \text{ nm}$ (where \hbar is the reduced Planck constant, and $D_{Al} = 2.25 \times 10^{-3} \text{ m}^2\text{s}^{-1}$ is the diffusion constant of the Al film). The Al/Cu bilayer forming S_2 shows a zero-temperature energy gap $\Delta_{0,2} \simeq 80 \mu\text{eV}$. S_2 lies within the Cooper limit, since $t_{Al} \ll \xi_{Al} \simeq 82 \text{ nm}$ and $t_{Cu} \ll \xi_{Cu} = \sqrt{\hbar D_{Cu}/(2\pi k_B T)} \simeq 127 \text{ nm}$ (where $D_{Cu} = 8 \times 10^{-3} \text{ m}^2\text{s}^{-1}$ is the diffusion constant of Cu, k_B is the Boltzmann constant and $T = 600 \text{ mK}$ is the highest operation temperature of the SQUID). Therefore, the superconducting coherence length of S_2 is $\xi_{S2} = \sqrt{\hbar(t_{Al} D_{Al} + t_{Cu} D_{Cu})/[(t_{Al} + t_{Cu})\Delta_{0,2}]} \simeq 190 \text{ nm}$.

Quasiparticle current in the S_1IS_2 junction

When the Josephson contribution is fully suppressed, by using a simple semiconductor model [45] it is straightforward to express the quasiparticle current in S_1IS_2 tunnel junctions as

$$I = \frac{1}{eR_T} \int_{-\infty}^{+\infty} d\epsilon N_1(\epsilon) N_2(\epsilon + eV) [f(\epsilon, T_1) - f(\epsilon + eV, T_2)], \quad (1)$$

where R_T is the normal-state resistance of the junction, e is the electron charge, V is the voltage drop across the junction, $N_i(\epsilon)$ and $f(\epsilon, T_i)$ (with $i = 1, 2$) are the quasiparticle density of states (DoSs) and the quasiparticle distribution functions, respectively. We work in the quasi-equilibrium regime [40, 41], where the electronic temperature

of each electrode is assumed to be well defined, and the occupation is expressed by the Fermi distribution function, $f(\epsilon, T_i) = [1 + \exp(\epsilon/k_B T_i)]^{-1}$. We assume a smeared BCS DoS for the superconducting i -lead, i.e., $N_i(\epsilon) = |\Re[(\epsilon + i\Gamma_i)/\sqrt{(\epsilon + i\Gamma_i)^2 - \Delta_i(T_i)^2}]|$, where $\Delta_i(T_i)$ is the temperature-dependent energy gap, and Γ_i is the Dynes parameter accounting for quasiparticle states within the energy gap [46]. The PH symmetry of the superconducting leads is reflected in the symmetry of the DoSs with respect to the energy, i.e., $N_i(\epsilon) = N_i(-\epsilon)$. By using this symmetry, it is straightforward to demonstrate the anti-symmetry of the tunnelling current, $I(-V) = -I(V)$. The essential features of the thermoelectric effect are well captured by this modeling [15], and the theoretical curves shown in Fig. 2a and b are obtained by fitting the experimental data with Eq. (1) (see SI for details). For two different superconductors with $\Delta_{0,1} > \Delta_{0,2}$ kept at the same temperature (i.e., for $T = T_1 = T_2$), the above expression predicts a purely dissipative behaviour. In the subgap regime [i.e., for $|eV| < (\Delta_1(T_1) + \Delta_2(T_2))$], the current is suppressed, and displays a matching peak at $V_p = \pm(\Delta_1(T_1) - \Delta_2(T_2))/e$ [50], whereas a sharp transition to the normal-state occurs at voltages $\pm(\Delta_1(T_1) + \Delta_2(T_2))/e$. In the presence of a temperature gradient or non-equilibrium, Eq. (1) admits also an *absolute negative conductance* (ANC) [42, 43], meaning that the current can flow against the voltage bias (i.e., $IV < 0$) hence acting as a thermoelectric generator. In particular, one can show that the S_1IS_2 system can generate thermoelectric power for $T_1 > T_2$ when the thermal gradient existing across the junction is sufficiently large ($T_1 > T_2\Delta_{0,1}/\Delta_{0,2}$) [15, 18]. Furthermore, the antisymmetry of the IV characteristic with voltage implies the peculiar *bipolarity* of this thermoelectric effect. The system shows optimal performance when the gap ratio fulfills the condition $\Delta_{0,2}/\Delta_{0,1} = 0.2 \div 0.5$. In addition, an increase of the temperature gradient is not necessarily beneficial for thermoelectricity, since this effect is strongly nonlinear. When the system is thermoelectric, there are, at least, two finite Seebeck. We observe that these Seebeck voltages are slightly larger than the value of the matching peak, i.e., $(\Delta_{0,1} - \Delta_{0,2})/e \lesssim |V_{th}^\pm|$ [15]. The maximum Seebeck voltages are mainly determined by the gap values, and they are only weakly-dependent on the thermal gradient occurring across the junction.

Seebeck coefficient

The Seebeck coefficient of a normal metal in the presence of energy-dependent scattering mechanisms (diffusive limit) can be calculated through the Mott-Jones equation [16], $\mathcal{S}_{linear} \simeq \left(\frac{\pi^2}{3}\right) \left(\frac{k_B}{e}\right) \left(\frac{k_B T}{E_{F,0}}\right) x$, where $E_{F,0}$ is the zero-temperature Fermi energy of the metal and $x = 2.78$ is a numerical constant that depends on the energy dependences of various charge transport parameters in Al. The resulting Seebeck coefficient of Al takes the values $S_{Al}(T = 300 \text{ K}) \simeq -1.74 \mu\text{V/K}$ and $S_{Al}(T = 650 \text{ mK}) \simeq -3.8 \text{ nV/K}$, where $E_{F,0} \simeq 11.6 \text{ eV}$. Since Al is typically superconducting at subKelvin temperatures, we can only theoretically estimate the Seebeck coefficient. Notably, experiments investigating Al at temperatures higher than its critical temperature reported values for the Seebeck coefficient of the same order of magnitude as the above theoretical estimate [17].

DATA AVAILABILITY

All other data that support the plots within this paper and other findings of this study are available from the corresponding author upon reasonable request.

ACKNOWLEDGEMENTS

The authors wish to thank for useful discussion Dr. T. Novotny, Dr. K. Michaeli, Prof. L. Amico, and Prof. F. Strocchi. We acknowledge the European Research Council under Grant Agreement No. 899315-TERASEC, and the EU's Horizon 2020 research and innovation program under Grant Agreement No. 800923 (SUPERTED) and No. 964398 (SUPERGATE) for partial financial support. A.B. acknowledges the SNS-WIS joint lab QUANTRA, funded by the Italian Ministry of Foreign Affairs and International Cooperation and the Royal Society through the International Exchanges between the UK and Italy (Grants No. IEC R2 192166 and IEC R2 212041).

AUTHOR CONTRIBUTIONS

F.P. fabricated the devices. G.G. and F.P. performed the experiments, and analysed the data with inputs from F.G.. G.M. and A.B. developed the theoretical model describing the experiment. All the authors wrote the manuscript.

F.P. and F.G. conceived the experiment. F.G. supervised and coordinated the project. All authors discussed the results and their implications equally at all stages.

ADDITIONAL INFORMATION

Supplementary Information is available for this paper.

Correspondence and requests for materials should be addressed to F.G..

The authors declare no competing interests.

-
- [1] Ashcroft, N., & Mermin, N., *Solid State Physics*. (Holt-Saunders, Philadelphia, 1976).
 - [2] Abrikosov, A. A. *Fundamentals of the Theory of Metals*. (Courier Dover Publications, 2017).
 - [3] Meissner, W. Z., Das elektrische Verhalten der Metalle im Temperaturgebiet des flüssigen Heliums. *Z. ges. Kälte-Industrie* **34**, 197 (1927).
 - [4] Ginzburg, V., On the thermoelectric phenomena in superconductors. *Zh. Eksp. Teor. Fiz.* **14**, 134 (1944).
 - [5] Guttman, G. D., Nathanson, B., Ben-Jacob, E., & Bergman, D. J., Thermoelectric and thermophase effects in Josephson junctions. *Phys. Rev. B*, **12** 691 (1997).
 - [6] Shelly, C. D., Matrozova, E. A. & Petrashov, V. T., Resolving thermoelectric "paradox" in superconductors. *Science* **2**, e1501250 (2016).
 - [7] Giazotto, F., Heikkilä, T. T., & Bergeret, F. S., Very Large Thermophase in Ferromagnetic Josephson Junctions. *Phys. Rev. Lett.* **114**, 067001 (2015).
 - [8] Kleeorin, Y., Meir, Y., Giazotto, F., & Dubi, Y., Large Tunable Thermophase in Superconductor – Quantum Dot – Superconductor Josephson Junctions. *Sci. Rep.* **6**, 35116 (2016).
 - [9] Smith, A. D., Tinkham, M., & Skocpol, W. J. New thermoelectric effect in tunnel junctions. *Phys. Rev. B* **22** 4346 (1980).
 - [10] Machon, P., Eschrig, M., & Belzig, W., Nonlocal thermoelectric effects and nonlocal Onsager relations in a three-terminal proximity-coupled superconductor-ferromagnet device. *Phys. Rev. Lett.* **110** 047002 (2013).
 - [11] Ozaeta, A., Virtanen, P., Bergeret, F. S., & Heikkilä, T. T., Predicted Very Large Thermoelectric Effect in Ferromagnet-Superconductor Junctions in the Presence of a Spin-Splitting Magnetic Field. *Phys. Rev. Lett.* **112**, 057001 (2014).
 - [12] Kolenda, S., Wolf, M. J., & Beckmann, D., Observation of Thermoelectric Currents in High-Field Superconductor-Ferromagnet Tunnel Junctions. *Phys. Rev. Lett.* **116**, 097001 (2016).
 - [13] Bergeret, F. S., Silaev, M., Virtanen, P., & Heikkilä, T. T., Colloquium: Nonequilibrium effects in superconductors with a spin-splitting field. *Rev. Mod. Phys.* **90**, 041001 (2018).
 - [14] Linder, J., & Robinson, J. W. A., Superconducting spintronics. *Nat. Phys.* **11**, 307-315 (2015).
 - [15] Marchegiani, G., Braggio, A., & Giazotto, F., Nonlinear Thermoelectricity with Electron-Hole Symmetric Systems. *Phys. Rev. Lett.* **124**, 106801 (2020).
 - [16] Mott, N. F., & Jones, H. *The theory of the properties of metals and alloys*. (Dover Publications, New York, 1958).
 - [17] Mamin, H. J., Clarke, J., & Van Harlingen, D. J., Charge imbalance induced by a temperature gradient in superconducting aluminum. *Phys. Rev. B* **29** 3881 (1984).
 - [18] Marchegiani, G., Braggio, A., & Giazotto, F., Superconducting nonlinear thermoelectric heat engine. *Phys. Rev. B* **101**, 214509 (2020).
 - [19] Marchegiani, G., Braggio, A., & Giazotto, F., Phase-tunable thermoelectricity in a Josephson junction. *Phys. Rev. Research* **2**, 043091 (2020).
 - [20] Giazotto, F., Paolucci, F., Braggio, A., Marchegiani, G., & Germanese G., Superconducting bipolar thermoelectric memory and method for writing a superconducting bipolar thermoelectric memory. Filing number: 102021000032042 (21/12/2021).
 - [21] Braginski, A. I., Superconductor Electronics: Status and Outlook. *J. Supercond. Nov. Magn.* **32**, 23-44 (2019).
 - [22] Ladd, T. D., Jelezko, F., Laflamme, R., Nakamura, Y., Monroe, C., & O'Brien, J. L., Quantum computers. *Nature* **464**, 45–53 (2010).
 - [23] Siddiqi, I., Engineering high-coherence superconducting qubits. *Nat. Rev. Mater.* **6**, 875 (2021).
 - [24] Polini, M., *et al.*, Materials and devices for fundamental quantum science and quantum technologies. *arXiv:2201.41299*88.
 - [25] Heikkilä, T. T., Ojajarvi, R., Maasilta, I. J., Strambini, E., Giazotto, F., & Bergeret, F. S., Thermoelectric Radiation Detector Based on Superconductor-Ferromagnet Systems. *Phys. Rev. Applied* **10**, 034053 (2018).
 - [26] Virtanen, P. & Heikkilä, T. T., Thermopower Induced by a Supercurrent in Superconductor–Normal-Metal Structures. *Phys. Rev. Lett.* **92**, 177004 (2004).
 - [27] Blasi, G., Taddei, F., Arrachea, L., Carrega, M. & Braggio, A. Nonlocal Thermoelectricity in a Superconductor–Topological-Insulator–Superconductor Junction in Contact with a Normal-Metal Probe: Evidence for Helical Edge States. *Phys. Rev. Lett.* **124**, 227701 (2020).
 - [28] Tan, Z. B., Laitinen, A., Kirsanov, N. S., Galda, A. Vinokur, V. M., Haque, M., Savin, A., Golubev, D. S., Lesovik, G. B. & Hakonen, P. J., Thermoelectric current in a graphene Cooper pair splitter. *Nat. Commun.* **12**, 138 (2021).

- [29] Eom, J., Chien, C.-J., & Chandrasekhar, V., Phase Dependent Thermopower in Andreev Interferometers. *Phys. Rev. Lett.* **81**, 437-440 (1998).
- [30] Jiang, Z., & Chandrasekhar, V., Quantitative measurements of the thermal resistance of Andreev interferometers. *Phys. Rev. B* **72**, 020502(R) (2005).
- [31] Hofstetter, L., Csonka, S., Nygård, J., Schönenberger, C., Cooper pair splitter realized in a two-quantum-dot Y-junction. *Nature* **461**, 960-963 (2009).
- [32] Benenti, G., Casati, G., Saito, K., & Whitney, R. S., Fundamental aspects of steady-state conversion of heat to work at the nanoscale. *Phys. Rep.* **694**, 1 (2017).
- [33] Campisi, M., Pekola, J. P., & Fazio, R., Nonequilibrium fluctuations in quantum heat engines: theory, example, and possible solid state experiments. *New J. Phys.* **17**, 035012 (2015).
- [34] Bera, M. L., Lewenstein, M. & Bera, M. N., Attaining Carnot efficiency with quantum and nanoscale heat engines. *npj Quantum Inf.* **7**, 31 (2021).
- [35] Josefsson, M., Svilans, A., Burke, A. M., Hoffmann, E. A., Fahlvik, S., Thelander, C., Leijnse, M., & Linke, H., A quantum-dot heat engine operating close to the thermodynamic efficiency limits. *Nature Nanotech.* **13**, 920 (2018).
- [36] Dubi, Y. & Di Ventra, M., Colloquium: Heat flow and thermoelectricity in atomic and molecular junctions *Rev. Mod. Phys.* **83** 131 (2011).
- [37] Ono, K., Shevchenko, S. N., Mori, T., Moriyama, S., & Nori, F., Analog of a Quantum Heat Engine Using a Single-Spin Qubit. *Phys. Rev. Lett.* **125**, 166802 (2020).
- [38] Kemppinen, A., Manninen, A., Möttönen, M., Vartiainen, J. J., Peltonen, J. T., & Pekola, J. P., Suppression of the critical current of a balanced superconducting quantum interference device. *Appl. Phys. Lett.* **92**, 052110 (2008).
- [39] Fornieri, A., Blanc, C., Bosisio, R., D'Ambrosio, S., & Giazotto, F., Nanoscale phase engineering of thermal transport with a Josephson heat modulator. *Nat. Nanotech.* **11**, 258-262 (2016).
- [40] Giazotto, F., Heikkilä, T. T., Luukanen, A., Savin, A. M., & Pekola J. P., Opportunities for mesoscopics in thermometry and refrigeration: Physics and applications. *Rev. Mod. Phys.* **78**, 217 (2006).
- [41] Fornieri, A., & Giazotto, F., Towards phase-coherent caloritronics in superconducting circuits. *Nat. Nanotechnol.* **12**, 944 (2017).
- [42] Aronov, A. G., & Spivak, B. Z., Photoeffect in a Josephson junction. *JETP Lett.* **22**, 101 (1975).
- [43] Gershenzon, M. E., & Falei, M. I., Absolute negative resistance of a tunnel contact between superconductors with a nonequilibrium quasiparticle distribution function. *JETP Lett.* **44**, 682 (1986).
- [44] Timofeev, A. V., Pascual Garcia, C., Kopnin, N. B., Savin, A. M., Meschke, M., Giazotto, F., & Pekola, J. P., Recombination-Limited Energy Relaxation in a Bardeen-Cooper-Schrieffer Superconductor. *Phys. Rev. Lett.* **102**, 017003 (2009).
- [45] Tinkham, M. *Introduction to Superconductivity* (McGraw-Hill, 1996).
- [46] Dynes, R. C., Garno, J. P., Hertel, G. B., & Orlando, T. P. Tunneling Study of Superconductivity near the Metal-Insulator Transition. *Phys. Rev. Lett.* **53**, 2437 (1984).
- [47] Bogoliubov, N. N., *Lectures on Quantum Statistics*. (Gordon and Breach, 1970)
- [48] Strocchi, F. *Symmetry Breaking*. (Springer, 2008).
- [49] Martinez-Perez, M. J., & Giazotto, F., A quantum diffractor for thermal flux. *Nat. Commun.* **5**, 3579 (2014).
- [50] Shapiro, S, Smith, P. H., Nicol, J., Miles, J. L., & Strong, P. F., Superconductivity and Electron Tunneling. *IBM J. Res. Dev.*, **6** 34 (1962)

SUPPLEMENTARY INFORMATION

I. MODEL OF THE DOUBLE-LOOP INTERFEROMETER

The interference pattern of a double-loop interferometer based on three tunnel Josephson junctions can be described by assuming a sinusoidal current-to-phase relation (CPR) for each junction and fluxoid quantization for the two loops. Therefore, the critical current of a double-loop interferometer can be written as [1-3]

$$I_C(\Phi) = \max_{\varphi_0} \left[I_0 \sin(\varphi_0) + I_A \sin\left(\varphi_0 + 2\pi \frac{\Phi_A}{\Phi_0}\right) + I_B \sin\left(\varphi_0 - 2\pi \frac{\Phi_B}{\Phi_0}\right) \right], \quad (2)$$

where φ_0 and I_0 are the phase drop and the critical current of the central junction, I_A is the critical current of the left junction, I_B is the critical current of the right junction, Φ_0 is the magnetic flux quantum, Φ_A is the magnetic flux piercing the left ring and Φ_B is the magnetic flux piercing the right ring. The total magnetic flux piercing the interferometer is $\Phi = \Phi_A + \Phi_B$. In order to take into account the asymmetry of the loop areas, we introduce the asymmetry coefficient α providing $\Phi_A = [(1 + \alpha)\Phi]/2$ and $\Phi_B = [(1 - \alpha)\Phi]/2$. By using the experimental values of $I_C(\Phi = 0)$ recorded at each temperature, we fit the interference patterns presented in Fig. 1e of the main text, thus estimating $\alpha = 0.003$, $r_A = I_A/I_0 = 0.63$ and $r_B = I_B/I_0 = 0.65$. We note that our device satisfies $|r_A - r_B| \leq 1$ and

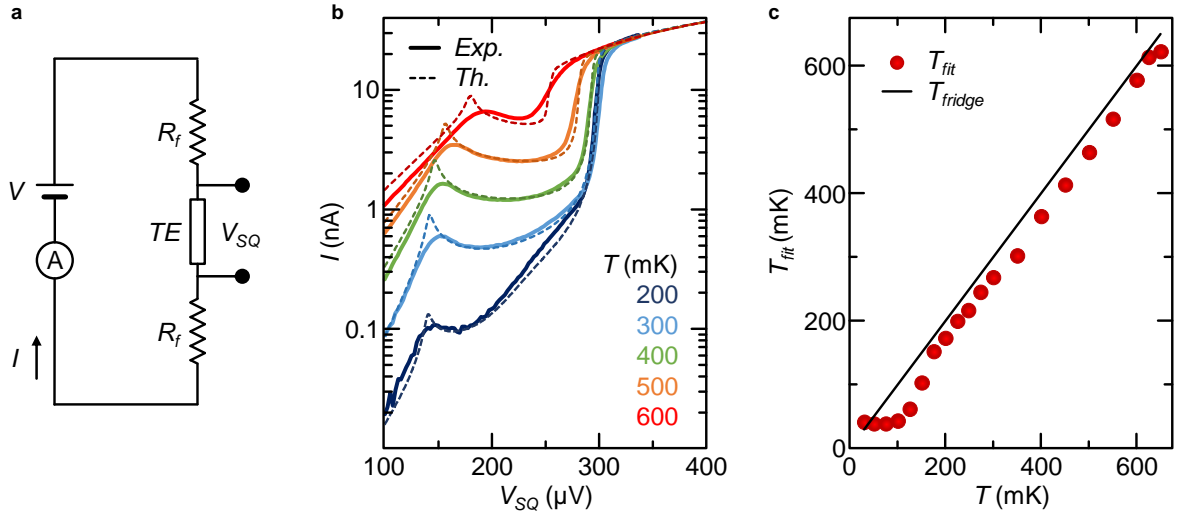


FIG. 5. **Equilibrium analysis of the current-voltage characteristics.** **a** Schematic electronic circuit for the measurement of the bipolar thermoelectric effect, where the thermoelectric element (TE) is in series with two RC filters present on each line of the dilution refrigerator. Here, V_{SQ} represents the voltage drop across the thermoelectric element (TE), I is the current, and $R_f = 1.1$ k Ω is the resistance of each filter. **b** Experimental $I(V_{SQ})$ characteristics (solid lines) plotted together with the fitted curves (dashed lines) for different values of bath temperature. **c** Temperature obtained from the fitting of the $I(V_{SQ})$ characteristics (T_{fit} , dots) and fridge temperature (T_{fridge} , line) for several measurements.

$r_A + r_B \geq 1$, therefore allowing to obtain perfect critical current suppression at specific values of Φ_A and Φ_B . Indeed, we measure a supercurrent suppression of about 1.75%.

II. ESTIMATE OF THE ELECTRONIC TEMPERATURE

The bipolar thermoelectric Josephson engine requires a finite temperature gradient to realize the thermoelectric effect. In the experiment, we do not directly measure the electronic temperatures of S_1 and S_2 (T_1 and T_2 , respectively). The theoretical curves displayed in Fig. 2a-b of the main text (dashed lines) are obtained through a two-parameter (T_1, T_2) fitting procedure performed on the current versus voltage characteristics under power injection. As we detail below, the main junctions parameters, such as the zero-temperature gaps of the two superconductors ($\Delta_{0,1}, \Delta_{0,2}$), are precisely estimated through a preliminary investigation of the equilibrium charge transport. In order to highlight the nature of the thermoelectric effect, we rely on a minimal model: we consider the quasiparticle current and replace the three junctions of the interferometer by a single junction with effective normal-state resistance R_T (the measured value of the normal-state resistance of the whole interferometer). The overall quality of the fits demonstrates the presence of the thermal gradient, and the robustness of the thermoelectric conversion with respect to unavoidable non-idealities present in the structure. The details of the model for quasiparticle transport in our systems are provided in the Methods section of the main text.

A. Equilibrium analysis

We measured the current-voltage tunnel characteristics $I(V)$ of the device for a zero input power ($P_{in} = 0$) at a magnetic flux $\Phi = 0.33\Phi_0$ (so to minimize the Josephson coupling). The measurement scheme is shown in Fig. 5a. As a first step, we observe that the voltage drop across the SQUID (V_{SQ}) is different from the measured value V , due to the presence of RC filters on the cryostat measurement lines. In particular, the SQUID voltage reads $V_{SQ} = V - 2R_f I(V)$, where $R_f = 1.1$ k Ω is the single filter resistance. The measured curves are shown in Fig. 5b in logarithmic scale (solid lines) for different values of bath temperature (T) in the range [30, 650] mK. The current is clearly non-monotonic in the voltage bias (V_{SQ}). The characteristics display a temperature-dependent peak structure for $V_{SQ} \sim V_p$, the "matching peak" in the jargon of the superconducting community, and an Ohmic behavior $I \sim V_{SQ}/R_T$ (with $R_T \simeq 9$ k Ω the total normal-state resistance of the SQUID) after a sharp current increase for $V_{SQ} \sim V_{max}$. In our modeling of the S_1IS_2 junction (see Eq. 1 of the main text), the values $V_p \sim [\Delta_1(T_1) - \Delta_2(T_2)]/|e|$, $V_{max} \sim [\Delta_1(T_1) + \Delta_2(T_2)]/|e|$ (with e the electron charge) yield information on the superconducting energy gap of S_1 and S_2 . Therefore, we

can immediately estimate the zero-temperature energy gaps $\Delta_{0,1} \sim 220 \mu\text{eV}$ and $\Delta_{0,2} \sim 80 \mu\text{eV}$, from the lowest temperature IV_{SQ} curves.

We make an *ansatz* for the temperature dependence of the gaps of S_1 , and S_2 , i.e., $\Delta_i(T) = \Delta_{0,i}\delta(T/T_{C,i})$ with $i = 1, 2$. Here, $\delta(T/T_{C,i})$ expresses the universal dependence [4] of the superconducting energy gap (in units of the zero-temperature value) as a function of the reduced temperature in the BCS weak-coupling limit. In particular, an approximate form of this numerical function is given by the expression $\delta(x) = \tanh(1.74\sqrt{x^{-1}-1})$, with a maximum deviation of the order of 2%. The critical temperatures of S_1 and S_2 were estimated experimentally as $T_{C,1} \sim 1.4 \text{ K}$, and $T_{C,2} \sim 625 \text{ mK}$, respectively. Notably, the S_1 gap-to-critical current ratio, $\Delta_{0,1}/(k_B T_{C,1})$, is very close to the BCS prediction, while $\Delta_{0,2}/(k_B T_{C,2})$ for the bilayer (S_2) deviates of about the 20%. This deviation may be ascribed to the spatial variation of the bilayer yielding a different gap amplitude at the three junctions (here treated as constant), or to the inverse proximity effect [5] which is used to properly engineer the gap, i.e., the film is a composite artificial superconductor. Finally, we need to establish the values of the Dynes parameters [6] in the smeared DoS of S_1 and S_2 . In our calculations, we set $\Gamma_1 = 2 \times 10^{-3}\Delta_{0,1}$, $\Gamma_2 = 2 \times 10^{-2}\Delta_{0,2}$, which guarantee a good matching between the IV_{SQ} experimental characteristics and the theoretical predictions, as we will see in the following.

In order to test the validity of the S_1IS_2 modeling and the parameters, we performed a one-parameter (T_{fit}) fit on the experimental curves, assuming thermal equilibrium $T_1 = T_2 = T_{\text{fit}}$. In the fitting procedure, we excluded the low-bias values ($V_{SQ} \rightarrow 0$), where the contribution of the residual Josephson effect can not be neglected. The IV_{SQ} characteristics fitted curves are shown in Fig. 5b (dashed lines) for different values of bath temperature. While the theoretical curves reproduce the overall behavior somewhat satisfactorily, we observe that the S_1IS_2 modeling of the IV_{SQ} characteristics leads to a systematic overestimate of the height of the matching peaks. This deviation is likely to be associated to our simplified modeling. Indeed, we consider a single junction instead of three (which may determine some inhomogeneity of the parameters among the different junctions) introducing a possible effective smearing parameter of the peaks which, for simplicity, we did not account here. Alternatively, this smearing in S_2 may be associated to the presence of the normal-metal Cu layer used to engineer the artificial superconductor.

Figure 5c displays the temperature (T_{fit} , points) obtained from the fit of the IV_{SQ} curves taken at different bath temperatures (T). The line $T_{\text{fit}} = T_{\text{fridge}}$ is also indicated for a comparison (solid line). The temperature profile is consistent with the fridge temperature with a good degree of accuracy. Significant deviations appear at lower temperatures ($T \lesssim 175 \text{ mK}$), where the signal becomes small (due to the exponential dependence of the $I(V_{SQ})$ characteristic on temperature of the electrodes) and more noisy, thus making a reliable fitting not possible. In summary, the equilibrium analysis demonstrates the possibility of extracting the electronic temperatures of S_1 , S_2 with good accuracy by fitting the IV_{SQ} characteristics.

B. Out-of-equilibrium Calibration

The values of the energy gaps and the Dynes parameters of the two superconductors (S_1 and S_2) forming the junctions were extracted from the analysis of the IV_{SQ} characteristics at thermal equilibrium, as discussed above. In this section, we fix these parameters ($\Delta_{0,1} \sim 220 \mu\text{eV}$, $\Delta_{0,2} \sim 80 \mu\text{eV}$, $\Gamma_1 = 2 \times 10^{-3}\Delta_{0,1}$ and $\Gamma_2 = 2 \times 10^{-2}\Delta_{0,2}$) and determine the temperatures T_1 and T_2 for values of the heating power (P_{in}) used in our experiments. To validate our analysis, we discuss two independent procedures: i) calibration of the hot temperature T_1 based on the P_{in} evolution of the gap threshold; ii) two-parameter (T_1 and T_2) fitting of the complete IV_{SQ} characteristics for different values of P_{in} .

1. Gap-sum threshold calibration

We start with the gap-threshold estimate of the temperature T_1 of the hot electrode (S_1). As discussed above, the gap-threshold bias voltage in the S_1IS_2 modeling is associated to the gaps sum, i.e., $V_{\text{max}} \sim [\Delta_1(T_1) + \Delta_2(T_2)]/|e|$. This quantity is extracted from the experimental curves as the maximum of the differential conductance curves, dI/dV_{SQ} . Figure 6 displays V_{max} as a function of the input power $P_{\text{in}} = V_{\text{in}}^2/2R_h$ (solid blue line), where $R_h = 51.8 \text{ k}\Omega$ is the normal-state series resistance of the two heaters. As expected, V_{max} decreases monotonically with P_{in} , since the energy gap $\Delta_1(T_1)$ is reduced due to the temperature increase. Here, we assume S_2 to be well thermalized at the lowest bath temperature so that its gap is well approximated by the zero-temperature value, $\Delta_2(T_2) \approx \Delta_{0,2}$. Within this approximation, the temperature T_1 of S_1 is obtained by solving the following equation:

$$|e|V_{\text{max}} = \Delta_{0,1}\delta(T_1/T_{C,1}) + \Delta_{0,2}. \quad (3)$$

The solution of Eq. 3 is displayed in Fig. 6 (solid red line). After a flat behaviour, $T_1(P_{\text{in}})$ increases monotonically

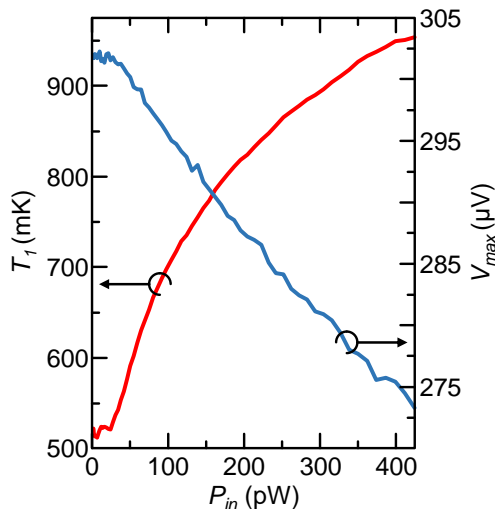


FIG. 6. **Gap-sum threshold calibration.** Blue curve: evolution of the voltage corresponding to the maximum of the differential conductance (V_{max}) as a function of the input power (P_{in}). Red curve: temperature T_1 of the hot superconductor (S_1) vs P_{in} obtained through a numerical solution of Eq. 3.

with the input power for $P_{in} = 22.5$ pW. We note that the following calibration is not reliable for small values of P_{in} . As a matter of fact, the temperature evolution of $\Delta_1(T_1)$ is exponentially suppressed for $T_1 \lesssim 0.4T_{C,1}$ so that it is fairly difficult to infer the correct hot temperature for those regimes giving the flat and noisy behaviour occurring for $P_{in} < 22.5$ pW.

2. Complete current-voltage characteristic calibration

We proceed now with a more refined calibration through numerical fitting of the complete current-voltage characteristic of the device. In the Methods section of the main text we provided the expression of the tunnelling current of the quasiparticle transport (Eq. 1 of the main text). Since we know the temperature dependence of the gaps (as discussed in the equilibrium analysis) and the Dynes parameters of S_1 and S_2 , the only two unknown quantities to fit the IV_{SQ} curves are the temperatures of the leads (T_1 and T_2).

The results of this fitting are shown in Fig. 7, where the temperatures T_1 and T_2 are plotted versus the input heating bias P_{in} (solid curves). The fitting procedure fails at very low injecting power, i.e., for $P_{in} < 10$ pW, where the $I(V_{SQ}, T_1, T_2)$ characteristic depends very weakly on T_1 and T_2 . We stress that the system is not thermoelectric for these low input powers. More precisely, the corresponding temperature gradient is insufficient to develop the nonlinear thermoelectricity in our device. As a result, the $I(V_{SQ})$ sensitivity with respect to the temperature difference is quite low. Instead, the temperature characterization (calibration) is significantly enhanced in the presence of thermoelectricity, which is signaled by the condition $IV_{SQ} < 0$. In such cases, the fitting returns the best values for the temperatures of the two leads. The temperature of S_1 increases monotonically with the input power from a minimum temperature $T_1(P_{in} = 22.5 \text{ pW}) \sim 0.65$ K to the value $T_1(P_{in} = 422.4 \text{ pW}) \sim 0.93$ K for the maximum power considered. Notably, the overall calibration is in good agreement with the previous estimation [$T_1(P_{in})$, dashed line] with a maximum difference of about 100 mK.

Moreover, the fitting procedure gives information about the temperature of the bilayer $T_2(P_{in})$. Interestingly, T_2 increases monotonically with P_{in} too (solid blue line). This behavior is associated with the heat-current flowing through the three junctions of the interferometer. This contribution represents the heat current transferred from the hot (S_1) to the cold (S_2) reservoir, as occurs in the operation of any standard thermodynamical engine. This interpretation could be further supported by imposing heat balance equations to the different parts of the system. Unfortunately, the complex geometry and the bilayer nature S_2 , combined with the unknown thermal coupling with the substrate, makes this procedure unfeasible. Notably, the maximum temperature of S_2 is about 0.35 K, where the gap is only slightly reduced with respect to the zero-temperature value $\Delta_2(T_2 = 0.35\text{K}) \sim 0.93\Delta_{0,2}$, thus justifying *a posteriori* the simplified approach that we followed in the previous section.

In conclusion, the presented calibration methods clearly demonstrate that there is a clear temperature gradient across the interferometer. In the curves (theoretical and experimental) for the nonlinear Seebeck coefficient (\mathcal{S})

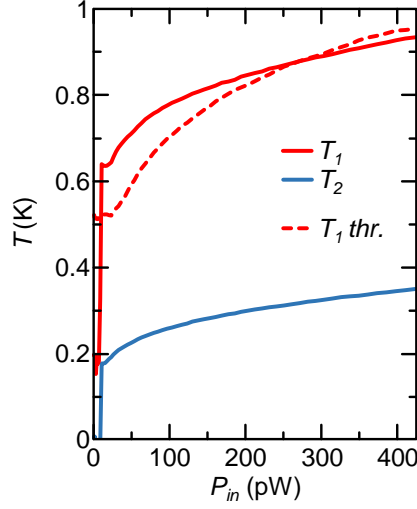


FIG. 7. **Complete current-voltage characteristic calibration.** Solid: temperature of the hot (T_1 , red) and the cold superconductors (T_2 , blue) as a function of the input power P_{in} . Dashed: the gap-sum calibration for the temperature of T_1 is displayed for a comparison.

displayed in Fig. 2c of the main text, we considered the two-parameter fitting calibration. In the previous analysis, we took conservative choices that may result in an overestimation of the thermal gradient in the junction. Thus, the estimated nonlinear Seebeck coefficient is possibly slightly underestimated, since \mathcal{S} is inversely proportional to the thermal gradient. Therefore, the real system may eventually even provide larger values of \mathcal{S} than the estimations reported in the main text.

III. HYSTERETIC TRANSPORT IN THE ENGINE CONFIGURATION

The electronic transport of the circuit implementing the bipolar thermoelectric Josephson engine (BTJE) shows a hysteretic behavior with the external bias current, as shown in Fig. 3c-d of the main text. The electronic circuit used to operate the BTJE is schematized in Fig. 8a. Here, the thermoelectric element is connected in series to the two low-pass filters placed in the lines of the cryostat ($R_f = 1.1 \text{ k}\Omega$). We note that I and V_{SQ} are the current and the voltage provided by the thermoelectric element, respectively. Furthermore, an external current generator (I_b) powers the parallel connection of the thermoelectric element and the load resistance (R_L). The charge transport in the circuit is described by the following system of relations:

$$\begin{cases} I_b = I_L + I & (a) \\ I_L = \frac{V_L}{R_L} & (b) \\ V_L = 2IR_f + V_{SQ} & (c) \end{cases} \quad (4)$$

where I_L is the current flowing through the load resistor and V_L is the associated voltage drop.

By substituting the Eq. 4a and b in Eq. 4c, we obtain the relation describing the direct-current steady state behavior of the circuit:

$$\begin{aligned} I &= -I_L + I_b \\ &= -\frac{V_L}{R_L} + I_b \\ &= -\frac{2IR_f + V_{SQ}}{R_L} + I_b \\ &= -\frac{V_{SQ}}{R_L + 2R_f} + \frac{R_L}{R_L + 2R_f} I_b. \end{aligned} \quad (5)$$

The result is a linear relation of $I(V_{SQ})$, where the load conductance ($\propto R_L^{-1}$) is the slope of the load-line and I_b is the intercept with I -axis taking into account $R_L \gg R_f$. Note that, due to the non-monotonic behaviour of $I(V_{SQ})$,

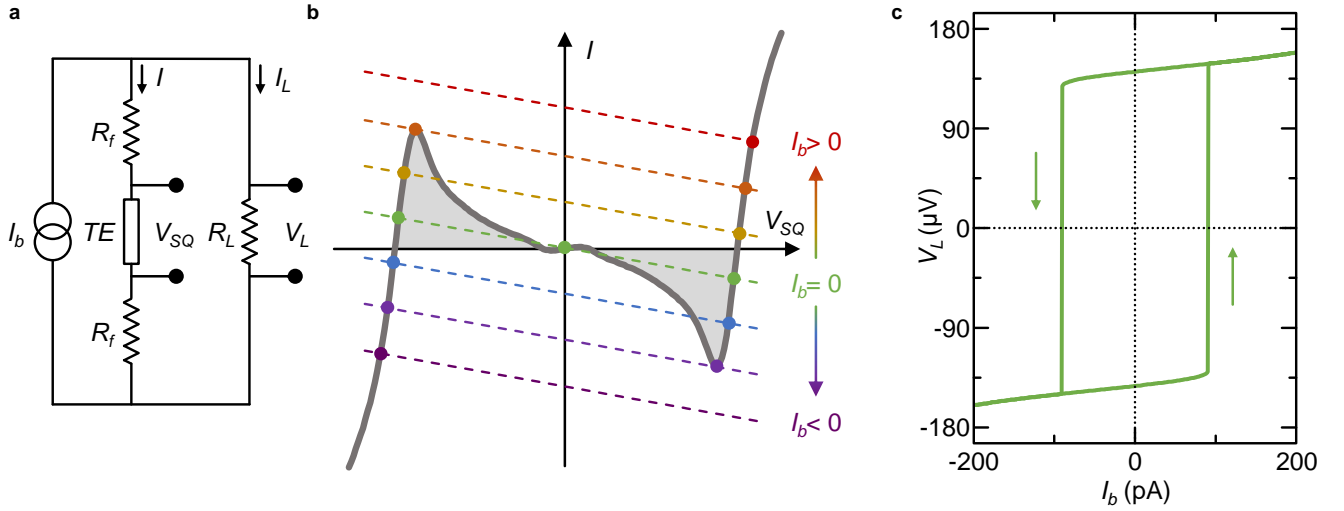


FIG. 8. **Power generation in the engine configuration.** **a** Schematic electronic circuit implementing the heat engine. The parallel between the load resistor (R_L) and the series of thermoelectric element (TE) and two filters (R_f) is biased by a dc current generator (I_b). V_L is the voltage measured across the load, while V_{SQ} is the voltage generated by the thermoelectric element. **b** Sketch of the current-voltage characteristic (IV_{SQ} , grey solid line) of the thermoelectric element intersected by a load-line for different positive and negative values of I_b . **c** Theoretical hysteresis curve obtained by solving Eq. 5 for $R_L = 2$ M Ω with the experimental IV_{SQ} of the thermoelectric element recorded at $P_{in} = 10$ pW.

the previous equations can admit multiple solutions. In order to have a stable-solution, the differential conductance at the crossing must be positive, as discussed in Refs. [15, 18].

Figure 8b displays a sketch of the current-voltage characteristic of the thermoelectric element crossed by the load resistance at different values of the bias voltage (see Eq. 5). By changing the bias current, the load-line sweeps the whole thermoelectric characteristic (dashed lines). The intersections between the two curves are highlighted with circles, which correspond to the solutions of Eq.(5) at different values of I_b . Thus, the theoretical curves describing the circuit in Fig. 8 can be directly obtained by substituting the measured $I(V_{SQ})$ characteristics in Eq. 5. In this way, we can obtain the hysteretical curves measured experimentally (see Fig. 3c-d of the main text). In particular, Fig. 8c shows the theoretical hysteresis curve obtained by solving Eq. 5 for $R_L = 2$ M Ω with the experimental thermoelectric characteristics recorded at $P_{in} = 10$ pW. Notably, by using the measured IV_{SQ} characteristic for the thermoelectric element, we can include also in the analysis the complex effects associated to the Josephson coupling. For example, a metastable state at $V \approx 0$ can be observed in the presence of Josephson coupling. Intriguingly, this simple analysis of the load-line is also able to predict the ignition of the thermoelectric elements. We will further investigate in detail this rich phenomenology in the following research.

A. Hysteresis curves for different loads

Intriguingly, the analysis of the hysteresis in the $I_b V_L$ characteristics can be easily applied to any value of load resistance. The experimental hysteresis curves resulting for five different nominal values of the load resistance are shown in Fig. 9a. Since the slope of the load-line depends strongly on the value of the load resistance used (R_L), low values of R_L do not cross the thermoelectric IV_{SQ} characteristics. This can be physically interpreted as the impossibility of the thermoelectric element to provide enough thermoelectrical power to the load. Indeed, this nonlinear thermoelectric effect necessarily produces a finite current to keep the spontaneous PH symmetry breaking, thus the element can clearly support a finite minimal load resistance. Differently, conventional linear thermoelectricity typically supports small loads by reducing the voltage and increasing the thermocurrent. The minimum value of the load resistance that can be supported by the junction is $R_{L,min} = V_p/I_p$ (with $\pm V_p$ and $\pm I_p$ the voltage and the current corresponding roughly to the thermoelectric peaks). In our case, the minimum load powered by the engine is $R_{L,min} = 0.8$ M Ω .

We can observe that the width of the hysteresis increases with the load resistance, while the values of voltage generated at $I_b = 0$ are almost independent from the load. The result is consistent with the previous discussion of Eq. 5. Indeed, for a larger R_L , the slope of the load-line is smaller. Thus, a larger bias current is needed to invert the

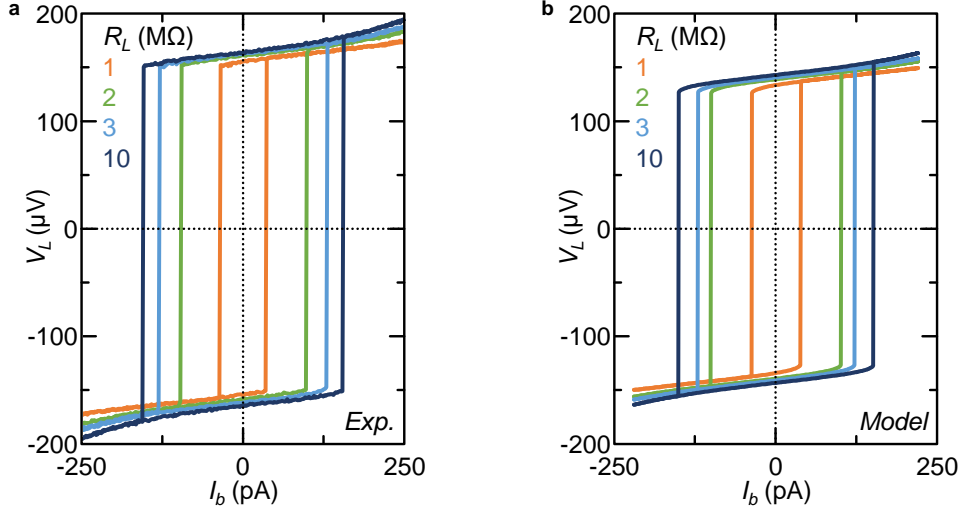


FIG. 9. **Hysteresis for different load resistors.** Experimental (a) and theoretical (b) hysteretic $V_L(I_b)$ curves for different values of the load resistance (R_L). The width of the hysteresis cycle in the four curves increases with R_L .

sign of the generated thermovoltage. Thus behavior is completely grabbed by the model describing the experimental circuit used to control the engine (see Fig. 8a). Indeed, the theoretical $V_L(I_b)$ curves obtained by solving Eq. 5 at a fixed input power show the same dependence on R_L (see Fig. 9b for $P_{in} = 10$ pW).

IV. ADDITIONAL THERMOELECTRIC DEVICE

To show the reproducibility of the effect, we tested and characterized also an additional device, which exhibits similar properties and behaviours. The additional device presents a similar design of Fig. (1c) of the main text. The details of the device fabrication and measurement set-up are quite the same of the sample used in the main text discussion and provided in the Methods section of the main text.

The two loops of the additional device show almost the same area, thus $\Phi_A = \Phi_B$. Furthermore, the same critical current flows through the two lateral arms, while the central Josephson junction has double the critical current ($r_A \sim r_B \leq 0.5$). In this way, the second and the third term of Eq. 2 are less relevant and contribute by increasing the minimum critical current of the interferometer. Figure 10 shows the equilibrium interference pattern of the additional device recorded at a bath temperature of 30 mK. The maximum critical current is $I_C \simeq 3.95$ nA, which is suppressed down to about 5%. This value of suppression is about one order of magnitude smaller than the value reached in the device shown in the main text. The minimum critical current is $I_C = 160$ pA recorded at $\Phi = 0.51\Phi_0$ (with Φ_0 the flux quantum).

Figure 10b shows the IV of the device recorded at $\Phi = 0.51\Phi_0$ and at a bath temperature of 30 mK for different values of input heating power (P_{in}). Differently from the device presented in the main text, the thermoelectric effect manifests in a smaller range of input power ($P_{in} = 8 - 90$ pW) due to the relevant presence of the Josephson current, which short-circuits the effect [9]. The maximum thermoelectric voltage is recorded at $P_{in} = 8$ pW and gets the value $V_{th} = \pm 141$ μ V, as shown in Fig. 10c. The thermoelectric voltage decreases by rising P_{in} , because the superconducting gap of the heated island [$\Delta_1(T_1)$] is reduced by the local heating. In addition, the gaps ratio [$\Delta_2(T_2)/\Delta_1(T_1)$] increases thus extinguishing the effect. We note that despite the Josephson coupling is larger than in the device presented in the main text, the overall behavior of the IV characteristics is qualitatively the same. Indeed, the Seebeck voltage has a very similar value and input power dependence even if in a smaller range of P_{in} .

We tested the additional device as BTJE by connecting the thermoelectric element in the circuit shown in Fig. 3a of the main text. The additional device shows the same qualitative behavior of the sample presented in the main text. Indeed, we obtained a hysteretic voltage-current characteristic, as shown in Fig. 10d for $R_L = 3$ M Ω and $P_{in} = 8$ pW at a bath temperature of 30 mK. The voltage across the load at zero bias current ($I_b = 0$), produced by the thermoelectric element, takes the value $V_L^\pm = \pm 158$ μ V. This value is very similar to the voltage of the matching peak [$(\Delta_{0,1} - \Delta_{0,2})/|e|$] and the voltage generated by the sample discussed in the main text. These voltages are given by the intersection between the load-line and the IV_{SQ} characteristic of the thermoelectric element. The details of the circuit piloting the engine are practically the same of the main text. The details are discussed in Sec. III of

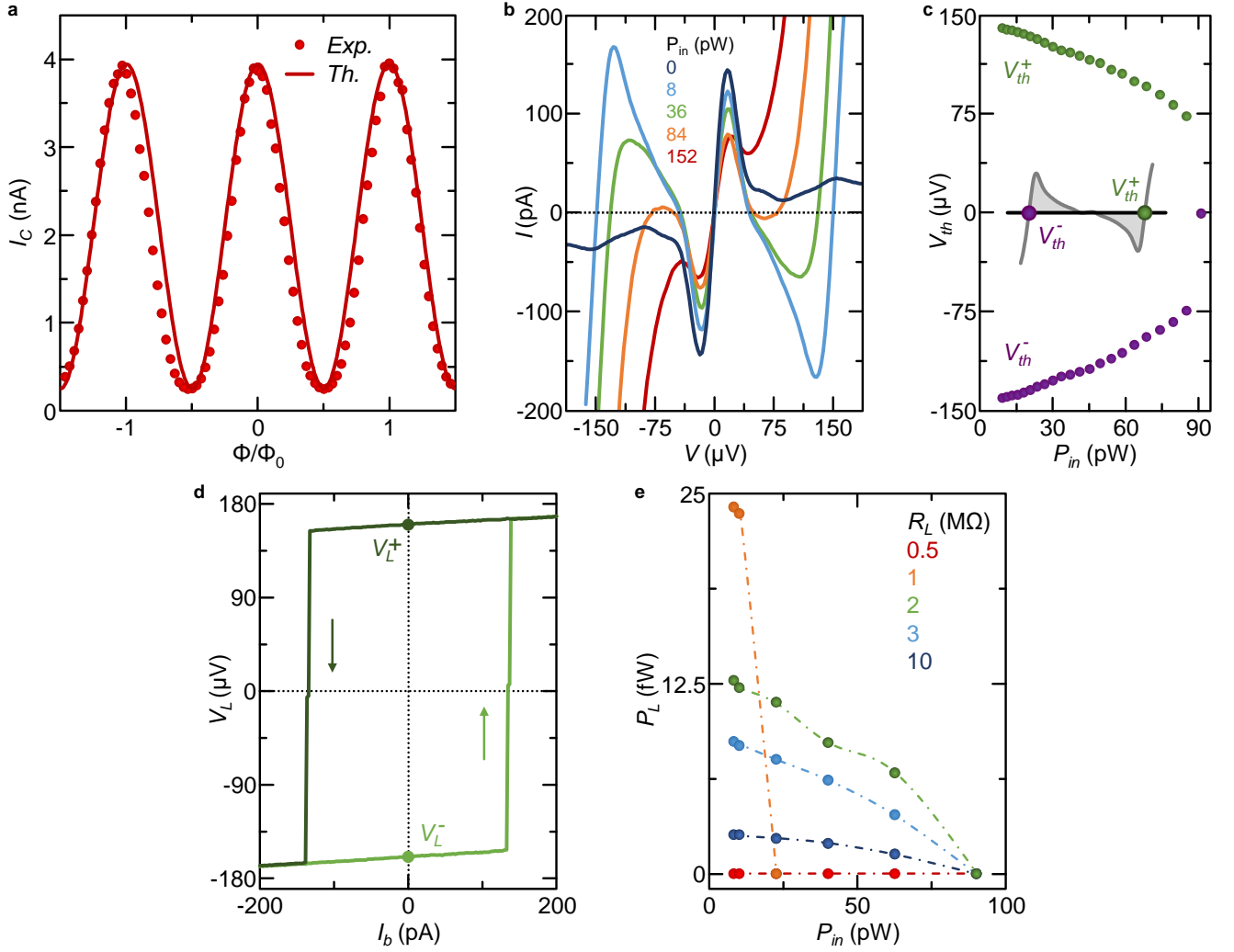


FIG. 10. **Properties of the additional thermoelectric device.** **a** Experimental interference pattern of a double loop SQUID (dots). The pattern shows a regular sinusoidal shape, getting a suppression of about 5% with respect to the maximum critical current. A fitting curve is reported (red line) by employing the model for a double loop SQUID (see Eq. 2). **b** Current-Voltage characteristic in the presence of a thermal bias recorded at $\Phi = 0.51\Phi_0$ and a bath temperature of 30 mK. The subgap IV curves are registered for different values of the power injection (P_{in}). Bipolar thermoelectricity is present in a restricted range of the input thermal power, that is $P_{in} = 8 - 90$ pW. **c** Thermoelectric voltage (V_{th}) as a function of P_{in} recorded at $\Phi = 0.51\Phi_0$ and bath temperature of 30 mK. The voltage gets a bipolar maximum value $V_{th} \simeq \pm 141$ μ V. **d** V_L versus I_b hysteresis curve recorded for $P_{in} = 8$ pW and $R_L = 3$ M Ω at a bath temperature of 30 mK. V_L^\pm are the voltage values generated by the heat engine at zero bias current ($I_b = 0$). **e** Engine output power generated on the load resistor (P_L) as a function of the injected power (P_{in}) recorded at a bath temperature of 30 mK for different values of R_L .

the Supplementary Information. We note that the width of the hysteresis is slightly larger than that of the device presented in the main text (see Fig. 10d), since the maximum thermoelectric current produced by the additional device is higher.

Figure 10e shows the output voltage power produced by the heat engine (P_L) as a function of P_{in} for different values of R_L . At a given value of P_{in} , P_L is larger for lower values of R_L but the engine operates in a narrower window of input powers, as recorded for the device shown in the main text. For $R_L = 0.5$ M Ω smaller than $R_{L,min} = 0.6$ M Ω , the engine does not produce any power on the load, as expected. Similarly to the other device, the maximum output electric power produced by this sample is about 24 fW for $R_L = 1$ M Ω .

The present discussion demonstrated the high reproducibility of the BTJE, since the additional device shows results very similar to the device discussed in the main text. This shows that the bipolar thermoelectricity induced by the spontaneous PH symmetry breaking is a large and robust effect. Indeed, the presence of the effect does not require a

fine tuning of the parameters when the Josephson coupling is sufficiently suppressed.

-
- [1] Kemppinen, A., Manninen, A., Möttönen, M., Vartiainen, J. J., Peltonen, J. T., & Pekola, J. P., Suppression of the critical current of a balanced superconducting quantum interference device. *Appl. Phys. Lett.* **92**, 052110 (2008).
 - [2] Ronzani, A., Altimiras, C., & Giazotto, F., Balanced double-loop mesoscopic interferometer based on Josephson proximity nanojunctions. *Appl. Phys. Lett.* **104**, 032601 (2014).
 - [3] Fornieri, A., Blanc, C., Bosisio, R., D'Ambrosio, S., & Giazotto, F., Nanoscale phase engineering of thermal transport with a Josephson heat modulator. *Nat. Nanotech.* **11**, 258–262 (2016).
 - [4] Tinkham, M. *Introduction to Superconductivity* (McGraw-Hill, 1996).
 - [5] de Gennes *Superconductivity of Metals and Alloys* (W. A. Benjamin, New York, 1966).
 - [6] Dynes, R. C., Garno, J. P., Hertel, G. B., & Orlando, T. P. Tunneling Study of Superconductivity near the Metal-Insulator Transition.
 - [7] Marchegiani, G., Braggio, A., & Giazotto, F., Nonlinear Thermoelectricity with Electron-Hole Symmetric Systems. *Phys. Rev. Lett.* **124**, 106801 (2020).
 - [8] Marchegiani, G., Braggio, A., & Giazotto, F., Superconducting nonlinear thermoelectric heat engine. *Phys. Rev. B* **101**, 214509 (2020).
 - [9] Meissner, W. Z., Das elektrische Verhalten der Metalle im Temperaturgebiet des flüssigen Heliums. *Z. ges. Kälte-Industrie* **34**, 197 (1927).